2014 IEEE International Conference on Robotics & Automation (ICRA)
Hong Kong Convention and Exhibition Center
May 31 - June 7, 2014. Hong Kong, China

# Software Compensation of Magnetic Crosstalk on Hall-Effect-based Rotary Encoders Close Together*

Guillaume Walck[1] and Veronique Perdereau[1]

***Abstract*— In the process of developing human-like robotic hands, engineers are looking for robust and accurate sensors that can fit in very confined spaces. Rotary encoders that measure joint angles of a multi-fingered hand must be of very small size and yet provide reliable and repetitive data. Hall-effect sensors combined with ring magnets fit in narrow spaces and have proved to be durable rotary magnetic position sensors due to their contact-less features. However, when several sensors of this kind are packed closely together in a finger, magnetic crosstalk effects appear and can lead to important errors/shifts in nearby sensor readings. This paper describes *magnetic crosstalk effects* in nearby joints and proposes a compensation method directly linked with the software calibration process.**

## I. INTRODUCTION

Measuring angular positions in robotics and more generally in industrial applications was solved with different types of sensors over the decades ranging from rotational potentiometers to optical sensors, from relative to absolute encoders. In robotic hand design, integrating an angular sensor into small-sized fingers is challenging. Potentiometers do not fit in the narrow phalanxes but solution based on optical sensors were proposed [1], [2]. However, these sensors are either influenced by ambient light [1] or add constraints for the light path [2]. Smaller than optical sensors, the Hall-effect-based rotary encoders used in the Shadow Dexterous robotic hand [3] completely fit inside the finger joints and are made absolute encoders by a combination of a permanent magnet and a Hall-effect sensor. Like optical encoders, they are not subject to friction and hence are more durable. Unfortunately, they suffer from one principal and known issue: their non-linearity. The Hall-effect sensor itself is also subject to drifts due to temperature variations but less than their resistive counter-parts. The magnetic sensing devices have evolved a lot [4]–[7] with different packages proposed to compensate intrinsic drawbacks, by integrating one or more Hall-effect cells, geometrically well placed, or by adding temperature measurement cells in the circuit directly. Moreover, the non-linearity of sensors in general, is now largely compensated with many possible solutions in different categories: (i) analog solutions that directly apply an inverse transfer function to provide an overall linear characteristic [8], (ii) ROM-based look-up tables and calibration techniques [9], [10] and (iii) advanced calibration algorithms [11], up to neural-network-based solutions [12].

*The research leading to these results has been supported by the HANDLE project (www.handle-project.eu), which has received funding from the European Community's Seventh Framework Program (FP7/2007-2013) under grant agreement: ICT 231640

[1]University Pierre and Marie Curie, 75005 Paris, France veronique.perdereau at upmc.fr

The problem treated in this paper deals with a less common disadvantage of these sensors that was encountered within the European project HANDLE. This project tackles the problem of in-hand manipulation with an anthropomorphic hand. The Shadow robotic hand used in the project is composed of 5 human-sized fingers (Fig. 1), each enclosing four Hall-effect-based rotary encoders. Some of the sensors show perturbing *magnetic crosstalk effects* due to the closely-packed magnets within different individual joints. This issue is particularly important when very small movements are required to perform fine in-hand manipulation. However, the problem is more generic and can appear in other devices using those kind of sensors working close together such as in an advanced joystick mentioned in [12].

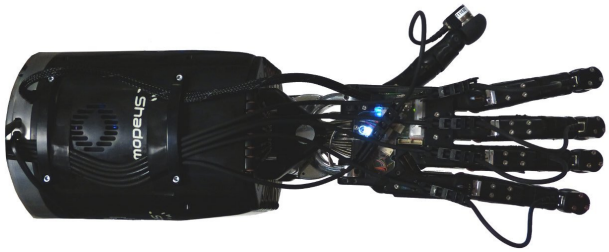


Fig. 1. Shadow Dexterous Hand used in the HANDLE project

Section II proposes a detailed description of the problem and explains the existing calibration technique used by the manufacturer. In section III, the novel compensation technique is described and a calibration process using visual markers is detailed. Results and comparison with the existing calibration method are given in section IV before section V concludes the paper.

## II. DESCRIPTION OF THE PROBLEM

The main advantage of rotary encoders based on magnetic effects is their contact-less characteristic. Nevertheless, the magnetic field produced in such sensors, useful to their function, can become a perturbation field, interacting at a distance with other elements in a close range. The *magnetic crosstalk effects* appear when other elements in the range are sensitive to the residual field.

### A. Sensors closely packed

The Shadow Dexterous hand is one of the most advanced robotic hand in the world with a total of 24 degrees of freedom (Fig. 2) and 20 motors (or 40 muscles in the pneumatic version). The device mimics the kinematics and

size of a human hand, and the actuation is based on tendons as on their biologic counter-parts, which makes it difficult to use motor-side optical encoders to derive the joint angles. Hence, the angular sensors are mounted on the finger joints directly. Because of the small size of the phalanxes, only magnetic angular sensing could be chosen, with several ring magnets and Hall-effect sensors tightly integrated in the finger links and joints (Fig. 3).

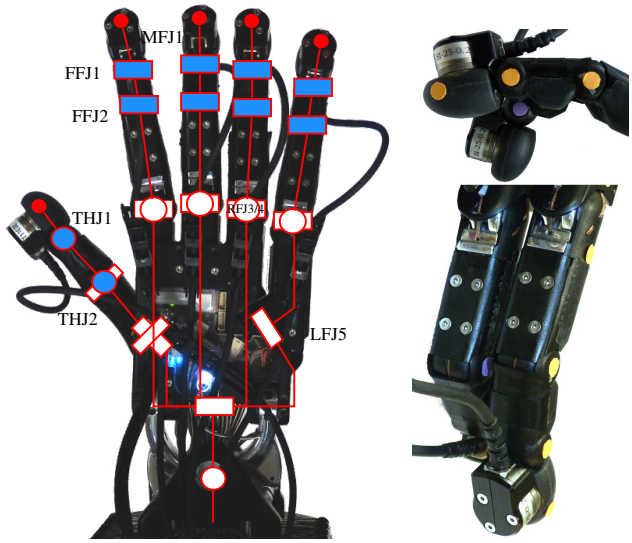


Fig. 2. (a) Kinematics of the Shadow hand, in blue, degrees of freedom with important crosstalk effects. (b) Nearby fingers close together.

The crosstalk effect that this paper is about, appears in almost all the successive joints separated by a link smaller than 30 mm (joints in blue on Fig. 2a). More rarely, there is also a magnetic influence on sensors when 2 adjacent fingers move close to each others, for example when the middle finger joint 2 (MFJ2) passes near the first finger joint 2 (FFJ2) (Fig. 2b). In this work, we focus on crosstalk problems of successive joints since they are permanent and dependent on 2 angles only, in each finger.

On figure 4, the raw ADC output readings of two adjacent Hall-effect sensors ($h_1$, $h_2$) in the thumb middle phalanx are shown for a variation of joint 1 over its working range (0°,90°). The influence of the magnet of joint 1 is noticeable on $h_2$ sensor reading and is more than 10 percent of $h_2$ full range of variation (80 units over 600 units). A similar but less important influence occurs on $h_1$ when joint 2 is moved in its smaller range (-38.5°,38.5°). Table I summarizes the influence each magnet has on a nearby sensor when relevant. Although J1 and J2 encoders are mutually influenced on each finger, one must note a non-negligible influence of little finger joint 5 (LFJ5), which is the palm pivot of the little finger metacarpal, on the ring finger knuckle joints (RFJ3/RFJ4). In fact, when LFJ5 increases, the magnets inside the little finger knuckle joint are completely moved away from the nearby sensors of the ring finger, producing

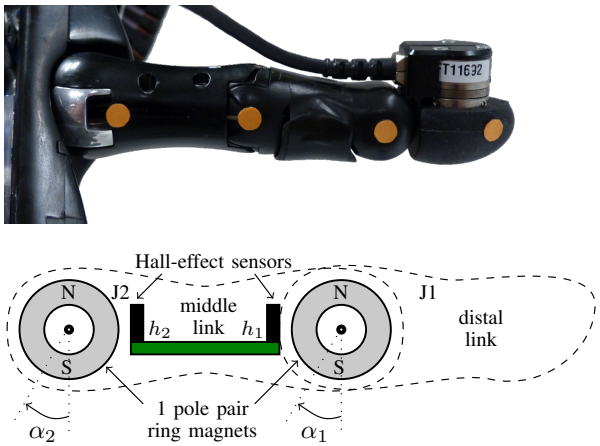


Fig. 3. Close-up view of the thumb and schematic view of the magnets inside THJ1 and THJ2 joints

an important shift. This effect is not seen on other knuckle encoders as the mutual constant influence is never moved away and is compensated by the calibration of each joint.

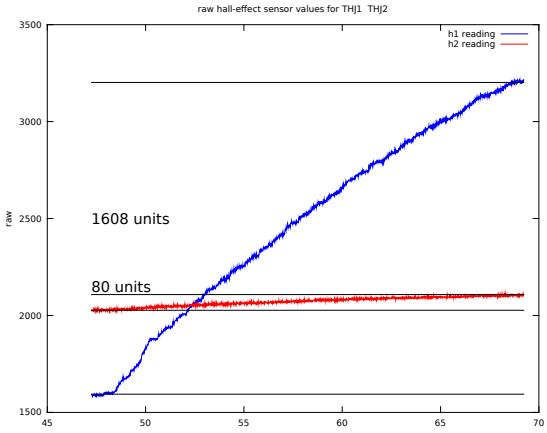


Fig. 4. Raw ADC output reading of 2 close Hall-effect sensor in the thumb for a variation of joint 1 (THJ1) over its full range

| sensor a | sensor b | a → b | b → a |
|---|---|---|---|
| THJ1 | THJ2 | 10% | 3.4% |
| THJ3 | THJ1 | 3.8% | ≈ 0 |
| (F/M/R/L)FJ1 | (F/M/R/L)FJ2 | 2.2% | 3.5% |
| LFJ5 | RFJ3/RFJ4 | 5% | ≈ 0 |

TABLE I

INFLUENCE (IN PERCENT OF THE VARIATION RANGE) OF ONE MAGNET TO AN ADJACENT SENSOR OVER ITS FULL RANGE

The most important crosstalk influence arises on joints 1 and 2 of the thumb. Indeed, the actual distance between the main magnet of joint 1 of the thumb (THJ1) and its Hall-effect sensor $h_1$ is 3 mm from the outer ring and 7 mm from the center. The Hall-effect sensor $h_2$ of joint THJ2 is at 11 mm from the outer ring of joint1 and 21 mm from its center. Due to this proximity, the THJ1 magnet influences sensor $h_2$ and THJ2 magnet influences sensor $h_1$. This means when

THJ2 is static and THJ1 moves, THJ2 is seen as moving by the system and vice-versa. The reason for that is the design of the existing calibration system relying on a single sensor and detailed here after.

### B. Current calibration method

Shadow Robot Company provides a ROS EtherCAT driver for their hand. Their driver (sr_edc_ethercat_driver) is responsible for transmitting data back and forth between the hand (palm firmware) and the software (realtime loop) on the host on which the device is connected. Angle measurements are transmitted at 1kHz as raw values coming from the Hall-effect sensors and converted through 12 bits ADCs (values between 0 and 4095). The calibration to true angles in radians is done inside the realtime loop using a calibration method based on look-up tables.

In fact, the calibration method performs a step-wise interpolation between 5 reference points read from a look-up table for each joint (Fig. 5). Calibration jigs permit to calibrate the joints, carefully creating the look-up table for each joint. None of the joints travel more than 90 degrees and the placement of the ring magnets is done such that the working zone is in the most linear part of the range (red on Fig. 5). Therefore the non-linearity is small and 5 points over the range has proven to be sufficient to keep the approximation error small. Without any perturbation and with some noise filtering, the precision of the calibrated rotary encoders is better than $\pm 0.5$ degrees.

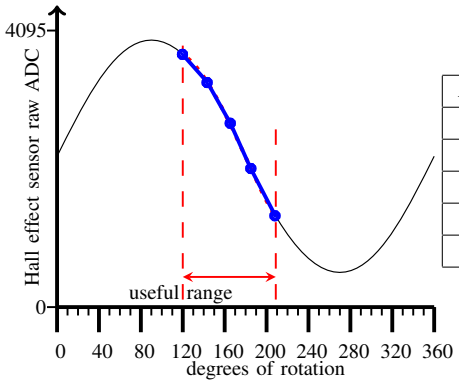


| ADC | angle |
|---|---|
| 3200 | 0 |
| 2921 | 22.5 |
| 2535 | 45 |
| 2110 | 67.5 |
| 1591 | 90 |

Fig. 5. Hall-effect sensor typical response with usesul range in red and step-wise linear interpolation in blue (left), look-up table example (right)

However, this method does not take into account the possible magnetic crosstalk perturbation of the adjacent joint although it is predictable. Indeed, the method relies only on the reading of the associated sensor and has no information about other movements of joints that influence its measurements.

The existing method leads to measurement errors up to 8 degrees in some joints, which is unacceptable for fine in-hand manipulation. With no possibility to modify the hardware, a new calibration technique, based on the reading of the 2 adjacent sensors was developed and is detailed in the next section.

## III. Calibration and Compensation

This section develops a solution for compensating the *magnetic crosstalk effect* on 2 adjacent joints and proposes a mean to implement it using a visual calibration technique.

To solve our problem, we took the advantage of having a host-side calibration for all the joints together rather than a firmware and/or chip-based calibration per joint. Indeed, the fact that all the Hall-effect sensors raw values are read at the same instant (iteration of the 1 kHz loop) makes it possible to do more complex computation on the complete set of data. The processing power and available memory to store larger look-up tables or compute inverse cosine functions was not an issue at all. Even if a large neural-network could be used to compensate all the effects (between two adjacent joints or adjacent fingers) with a method similar to [12], the proposed solution handles each finger separately since the largest crosstalk effects are only on adjacent joints J1/J2. Two adjacent sensors are processed to compensate the influence of one magnet on the second sensor and vice versa.

### A. Physical model

Let us present the problem related to the physics of magnetic interaction. We suppose the ring magnets can be represented as perfect magnetic dipoles with a magnetic moment $\vec{M}_i$. Figure 6 shows the magnetic field $\vec{B}_i$ seen at point $P_i$ by one of the ring magnet. The Hall-effect sensor measures the field in one direction only, along the segment $O_iP_i$. One must consider $B_{r,i}$, the projection of $\vec{B}_i$ on this segment. $\alpha_i$ is the joint angle chosen by Shadow Robot.

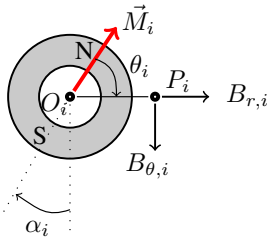


Fig. 6. Magnetic field created by a ring magnet equivalent to a dipole

In polar coordinates $(\theta_i, r_i)$, $B_{r,i}$ depends on the distance $r_i$ from the center $O_i$ and on the angle $\theta_i$ with the magnetic moment as expressed in the following equation:

$$B_{r,i} = C_i \frac{2cos(\theta_i)}{r_i^3} = C_i \frac{2sin(\alpha_i)}{r_i^3} \quad (1)$$

with constant $C_i$ depending on moment $\vec{M}_i$ and vacuum permeability $\mu_0$, since permanent magnets are used.

Considering a pair of magnets placed in the same configuration as on adjacent joints in the robot hand, we can derive the magnetic field at point $P_2$, center of the Hall-effect sensor of joint 2, as the sum $B_r$ of the influence of the 2 magnets (Fig. 7). $B_{r,1}$ and $B_{r,2}$ are the projections of the magnetic field of each magnet on the axis linking both joints, and depend each one on the angle and radius to their

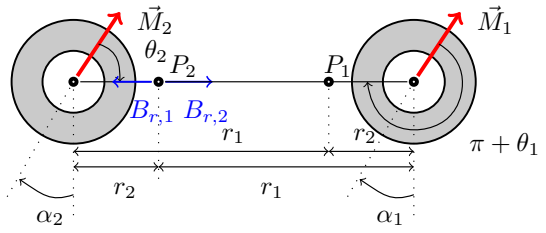


Fig. 7. Magnetic field created by 2 adjacent ring magnets

respective magnetic moments. Resulting field $B_r\mid_{P_2}$ at $P_2$ is then:

$$B_r\mid_{P_2} = C_2\frac{2sin(\alpha_2)}{r_2^3} - C_1\frac{2sin(\alpha_1)}{r_1^3} \tag{2}$$

with $C_1$ and $C_2$ the constants depending on the ring magnets characteristics. Even if there are other phenomena that were ignored (printed board circuit and screws in the regions of the magnet), we clearly have a Hall-effect sensor reading dependent on both angles. Because the sensor placement is symmetrical, the relation is true at both sensor centers, so we also have:

$$B_r\mid_{P_1} = C_1\frac{2sin(\alpha_1)}{r_2^3} - C_2\frac{2sin(\alpha_2)}{r_1^3} \tag{3}$$

To simplify the notation, we note $h_1$ (resp. $h_2$) the value of $B_r\mid_{P_1}$ (resp. $B_r\mid_{P_2}$) measured by the Hall-effect sensors at $P_1$ (resp. $P_2$). We extract $\alpha_1$ and $\alpha_2$ from Eq. 2 and Eq. 3:

$$sin(\alpha_2) = \left(h_2 + \frac{2C_1 sin(\alpha_1)}{r_1^3}\right)\frac{r_2^3}{2C_2} \tag{4}$$

$$sin(\alpha_1) = \left(h_1 + \frac{2C_2 sin(\alpha_2)}{r_1^3}\right)\frac{r_2^3}{2C_1} \tag{5}$$

As mentioned earlier, the measurements of both sensors are available at the same time. It is then possible to express the angles by combining equations Eq. 4 and Eq. 5:

$$\alpha_1 = arcsin\left(\left(\frac{1}{1-\left(\frac{r_2}{r_1}\right)^6}\right)(a_1h_1 + a_2h_2)\right) \tag{6}$$

with $a_1 = \frac{r_2^3}{2C_1}$ and $a_2 = \frac{r_2^6}{2C_1r_1^3}$.

A similar expression can be found for $\alpha_2$:

$$\alpha_2 = arcsin\left(\left(\frac{1}{1-\left(\frac{r_2}{r_1}\right)^6}\right)(a_3h_2 + a_4h_1)\right) \tag{7}$$

with $a_3 = \frac{r_2^3}{2C_2}$ and $a_4 = \frac{r_2^6}{2C_2r_1^3}$.

Finally, we managed to get a relationship between a joint measurement and 2 adjacent sensor readings, taking into account the mutual influence of the packed pair of magnets. However, to compute the angles effectively, all the constants should be known. There is no easy mean to precisely extract each single constant, but a parameter fitting method based on real measurements and reference values can solve this problem.

### B. Model-based approach

The host side calibration software can easily compute the angle values through a model. Since the exact model (Eq. 6, Eq. 7) is non-linear, we checked several approximated linear models with increasing complexity from 3 to 7 parameters per joint, and tried to find the parameters via a fitting method. For each case, we considered a linear regression fitted with the least squares approach.

*1) Linear model:* Knowing that $\alpha_1$ (resp. $\alpha_2$) builds up as the sum of 2 sensor values led us to first coarsely approximate the equations with a linear model with 3 parameters per joint:

$$\alpha = c_0 + c_1h_1 + c_2h_2 \tag{8}$$

*2) Polynomial models:* To add complexity, several polynomial models were tested such as this example:

$$\alpha = c_0 + c_1h_1 + c_2h_2 + c_3h_1^3 + c_4h_2^3 \tag{9}$$

5 parameters are required per joint in this model.

*3) Taylor series decomposition model:* A more precise approximated model comes from the Taylor series of the trigonometric function $arcsin$:

$$arcsin(x) = \sum_{n=0}^{\infty}\frac{(2n)!}{4^n(n!)^2(2n+1)}x^{2n+1} \text{ for } \mid x \mid < 1 \tag{10}$$

The 2nd-degree Taylor polynomial of $arcsin$ gives a polynomial model of degree 3:

$$arcsin(x) \approx 1 + x + \frac{x^3}{6} \tag{11}$$

By replacing $x = (h_1 + h_2)$ we obtain a new model:

$$\alpha = c_0 + c_1h_1 + c_2h_2 + c_3h_1^3 + c_4h_2^3 + c_5h_2h_1^2 + c_6h_1h_2^2 \tag{12}$$

It includes crossed-terms and leads to 7 parameters per joint.

To get good results in the linear regressions with our different models, the number of ground-truth values must be important, even more when the number of parameters to find is high. Obtaining those reference values is described in the next subsection.

### C. Ground-truth extraction

A large number of reference points must be extracted to correctly fit the model. We remind that only 5 calibration jigs are provided per joints, which means 25 points can be measured theoretically for 2 adjacent joints. Unfortunately, the calibration jigs were not designed to fit simultaneously on the joints as they both use the same leaning surfaces to be accurately placed. So a new technique had to be proposed, not using the jigs and preferably providing more points.

A visual reference angle extraction method was created, using the joint center screws as markers for a circle extraction technique. The angles between the lines connecting the circle centers give the joint angles. Such a method is robust to the placement of the camera if the image plane is roughly parallel to the finger plane and if the finger is close to the center of the image. The existing screws are not all shiny and easy to segment, so, some color markers were added in a first step,

directly over the screw heads, making it easier to distinguish their centers (Fig. 3).

The processing chain is shown in figure 8 and was implemented in OpenCV [13]. In an initialization phase, the

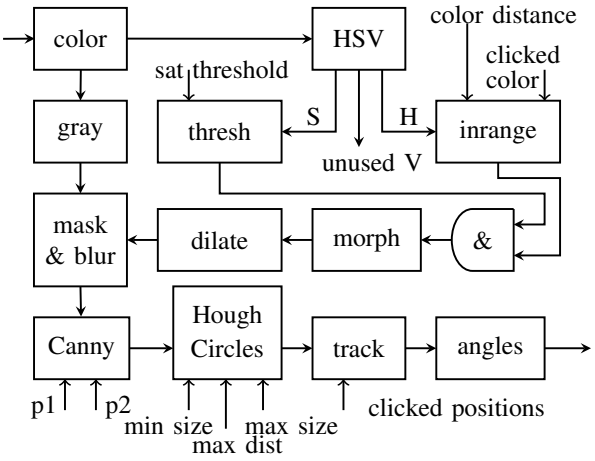


Fig. 8. Angle extraction processing chain

user clicks the color markers on the joints in the correct order. Thanks to a color segmentation on the hue channel in hue-saturation-value (HSV) color-space, a dilated mask is created and applied to the gray image to get a perfect circle contour extraction through a Canny filter (p1 and p2 are the filter hysteresis thresholds). The Hough transform for circles is applied to get the circle centers for a radius in a given range. Tracking of the circles is done to keep the same order and association of the centers with the joint numbers. The joint angles between connected centers are then computed (Fig. 9).

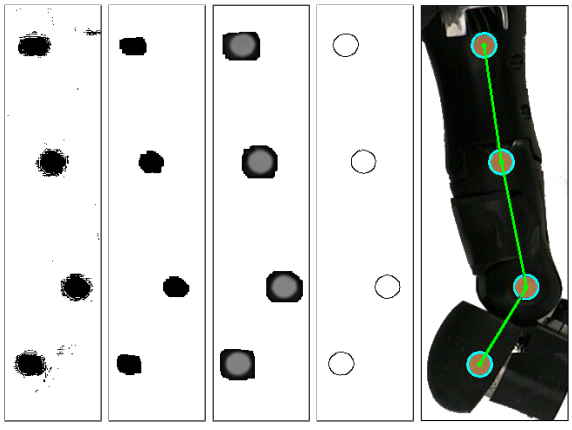


Fig. 9. Processing example: (a) color segmentation, (b) morphology close, (c) dilated mask on grayscale, (d) Canny filter, (e) final result after tracking

The obtained angles have been checked against the calibration jigs and are correct within $\pm 0.5$ degrees when the segmentation and filter parameters are tuned properly. When used simultaneously, the calibration jigs do not offer a better precision whereas our method can virtually provide as many reference points as required. With this method, data from 60 positions were extracted, covering the entire range of both J1 and J2 joints, essentially by moving each joint independently for several fixed positions of the adjacent joints. Both raw values and reference angles were stored to be processed by the model-fitting method.

### D. Model-fitting

To extract the model parameters, we used a model-fitting technique. Basically, we solve the system for $N$ samples per joint. Let us illustrate the algorithm with the first polynomial model (Eq. 9) on $\alpha_1$:

$$\begin{cases} \alpha_{1,1} &= c_0 + c_1 h_{1,1} + c_2 h_{2,1} + c_3 h_{1,1}^3 + c_4 h_{2,1}^3 \\ \vdots &= \vdots \\ \alpha_{1,N} &= c_0 + c_1 h_{1,N} + c_2 h_{2,N} + c_3 h_{1,N}^3 + c_4 h_{2,N}^3 \end{cases} \tag{13}$$

The regression was implemented thanks to a matrix format. We obtain:

$$\begin{bmatrix} \alpha_{1,1} \\ \vdots \\ \alpha_{1,N} \end{bmatrix} = \mathbf{H}. \begin{bmatrix} c_0 \\ \vdots \\ c_4 \end{bmatrix} \tag{14}$$

with,

$$\mathbf{H} = \begin{bmatrix} 1 & h_{1,1} & h_{2,1} & h_{1,1}^3 & h_{2,1}^3 \\ \vdots & \vdots & \vdots & \vdots & \vdots \\ 1 & h_{1,N} & h_{2,N} & h_{1,N}^3 & h_{2,N}^3 \end{bmatrix} \tag{15}$$

Then,

$$\mathbf{C} = [c_0, \cdots, c_4]^\top = \mathbf{H}^\dagger . [\alpha_{1,1}, \cdots, \alpha_{1,N}]^\top \tag{16}$$

with $\mathbf{H}^\dagger$ the pseudo-inverse of $\mathbf{H}$.

Once the parameters $\mathbf{C}$ are computed, they are saved in a configuration file to be used by the driver. The calibration function integrated in the main loop of the driver was modified to apply the selected model to the calibration of each pair of adjacent joints.

## IV. Results and Comparison

Figure 10 shows how one of our models fits well on angle J1 reference values compared to the Shadow calibration when J2 was static at 38.5 degrees. The differences are mainly at the extreme parts of the range, better fitted by our polynomial model with higher degree and cross-terms. The coefficients $c_0, \cdots, c_6$ found for this example are $1.8, -7.1 * 10^{-4}, 7.2 * 10^{-4}, 0.52, -9.7, -1.9 * 10^{-3}, 3.0 * 10^{-3}$.

In order to evaluate the results, two criteria were used:

- determination coefficient $R^2$ over the model-fitting
- amplitude and mean errors in the sensor range

First the models were compared with respect to the determination coefficient, measuring how close the model is from the recorded data (1.0 being a perfect match). Table II gives $R^2$ for each model.

Naturally, the model from the Taylor series, derived from the physics of magnetic interaction, achieves the best fitting results. Other polynomial models not including crossed-terms do not improve the result. For every model, the

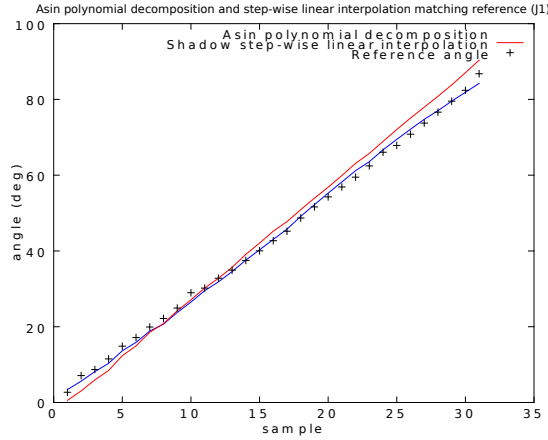


Fig. 10. Model-fitting on the raw sensor data with the Taylor series model (blue) and with the Shadow calibration (red) for joint 1 when $\alpha_2$ was static at 38.5°

| | linear | polynomial | polynomial (Taylor) |
|---|---|---|---|
| $R^2$ for $\alpha_1$ | 0.9920 | 0.9975 | **0.9989** |
| $R^2$ for $\alpha_2$ | 0.9990 | 0.9995 | **0.9997** |

TABLE II

DETERMINATION COEFFICIENT $R^2$ FOR EACH MODEL FOR BOTH ANGLES

regression for $\alpha_1$ is worse than for $\alpha_2$ because joint 1 has a larger range of motion and the model may not capture the variations at the end of the range.

An analysis of the amplitude of the errors over the range between the computed joint angles and the reference angles extracted by our visual-based method is given in table III for our best model (polynomial Taylor) and for the Shadow calibration. The errors are different on joint 1 and joint 2 depending on the type of movements of the adjacent joint, so only the largest error amplitude is shown.

| range of motion | error Taylor | error Shadow |
|---|---|---|
| $\alpha_1 \in$ [0;90], $\alpha_2$=0 | 2.22° | 8.16° |
| $\alpha_1 \in$ [0;90], $\alpha_2$=38.6 | 4.27° | 9.69° |
| $\alpha_1 \in$ [0;90], $\alpha_2$=-38.6 | 3.98° | 9.10° |
| $\alpha_2 \in$ [-38;38], $\alpha_1$=0 | 3.47° | 4.79° |

TABLE III

COMPARISON OF LARGEST ERROR AMPLITUDE AMONG BOTH ANGLES

Our model-based approach of the calibration gives always better results than the calibration with look-up tables used by the manufacturer. Improvements range from a factor of 1.3 to 3.6 on the largest error amplitude. It is important to note that the majority of the in-hand movements performed by the fingers do not travel the whole range of the joint, so the maximum amplitude of the error is not sufficient to evaluate the performance of the new compensation method. We also considered the mean absolute error over the range. The largest mean error among both angles for our method in comparison to Shadow's mean error is presented in table IV.

The results are even more interesting on the mean error since we obtain a mean error more than 5 times better in one scenario and twice better in the worst case.

| range of motion | mean error Taylor | mean error Shadow |
|---|---|---|
| $\alpha_1 \in$ [0;90], $\alpha_2$=0 | 0.59° | 3.15° |
| $\alpha_1 \in$ [0;90], $\alpha_2$=38.6 | 0.97° | 3.8° |
| $\alpha_1 \in$ [0;90], $\alpha_2$=-38.6 | 0.74° | 4.17° |
| $\alpha_2 \in$ [-38;38], $\alpha_1$=0 | 0.75° | 1.44° |

TABLE IV

COMPARISON OF LARGEST MEAN ERROR AMONG BOTH ANGLES

## V. CONCLUSION

In the context of in-hand manipulation with a robot hand, a *magnetic cross-talk effect* between adjacent sensors packed closely together appears and leads to important errors in nearby sensor readings. A solution compensating the perturbation was proposed and integrated within a two-phase calibration process. In the first phase, a visual angle extraction technique was created to capture more reference points than standard calibration using jigs. Such a method can be used with other procedures that require reference angles and could even be automatic provided that segmentation of intrinsic features of the robot finger is improved.

In a second phase, a model-based technique, derived from the physics of magnetic interaction, was used to calibrate adjacent sensors. Significant results were achieved in comparison with the existing solution with an improvement factor from 2 to 5 on the errors. Further work will be done on other crosstalk effects such as those in sensors of nearby fingers.

## REFERENCES


[1] A. Cavallo, G. D. Maria, C. Natale, and S. Pirozzi, "Optoelectronic joint angular sensor for robotic fingers," *Sensors and Actuators A: Physical*, vol. 152, no. 2, pp. 203 – 210, 2009.

[2] G. Palli and S. Pirozzi, "Optical sensor for angular position measurements embedded in robotic finger joints," *Advanced Robotics*, vol. 27, no. 15, pp. 1209 – 1220, 2013.

[3] Shadow Robot Company, "Shadow ethercat dual can motor hand." http://www.shadowrobot.com.

[4] E. R. Strandt, "Hall-effect incremental angle encoder," *IEEE Transactions on Instrumentation and Measurement*, vol. 12, no. 1, pp. 22–26, 1963.

[5] M. Poole and R. Walker, "Hall effect probes and their use in a fully automated magnetic measuring system," *IEEE Transactions on Magnetics*, vol. 17, no. 5, pp. 2129–2132, 1981.

[6] R. Popovic, Z. Randjelovic, and D. Manic, "Integrated hall-effect magnetic sensors," *Sensors and Actuators A: Physical*, vol. 91, no. 1–2, pp. 46 – 50, 2001.

[7] S. Lozanova and C. Roumenin, "Angular position device with 2d low-noise hall microsensor," *Sensors and Actuators A: Physical*, vol. 162, no. 2, pp. 167 – 171, 2010. Eurosensors XXIII, 2009.

[8] F. Trofimenkoff and R. E. Smallwood, "Analog-multiplier circuit linearizes transducer output," *IEEE Transactions on Instrumentation and Measurement*, vol. 23, no. 3, pp. 195–197, 1974.

[9] G. Kondraske and R. Ramaawamy, "A microprocessor-based system for adaptable calibration and linearization of hall-effect position sensors," *IEEE Transactions on Instrumentation and Measurement*, vol. IM-35, no. 3, pp. 338–343, 1986.

[10] M. Kayal and M. Pastre, "Automatic calibration of hall sensor microsystems," *Microelectron. J.*, vol. 37, pp. 1569–1575, Dec. 2006.

[11] J. Rivera, G. Herrera, and M. Chacón, "Improved progressive polynomial algorithm for self-calibration and optimal response in smart sensors," *Measurement*, vol. 42, no. 9, pp. 1395 – 1401, 2009.

[12] G. Northey, M. Oliver, and D. Rittenhouse, "Calibration of a hall effect displacement measurement system for complex motion analysis using a neural network," *Journal of Biomechanics*, vol. 39, no. 10, pp. 1943 – 1947, 2006.

[13] G. Bradski, "The OpenCV Library," *Dr. Dobb's Journal of Software Tools*, 2000.